relapse and NR). Cumulative development of HCC based on serum AFP level (<10 ng/ml vs. ≥10 ng/ml) at EOT was determined by the Kaplan–Meier method. Differences between the curves were evaluated by log-rank test. Statistical analyses were performed by SPSS 15.0 (SPSS Japan Inc., Tokyo, Japan). A *P*-value of <0.05 was considered statistically significant.

Results

Clinical Features of Patients Classified by Serum AFP Level at Baseline

A total of 263 patients were studied. The mean AFP level (mean ± SD) at baseline was 15.0 ± 41.9 ng/ml, and the median was 5.1 ng/ml (range, 1.0–542.0). There were 71 patients with serum AFP ≥10 ng/ml at baseline (27.0%). The serum AFP level usually remained elevated without large fluctuations, although the evident pattern of AFP elevation varied in each patient. Clinical features of patients classified by serum AFP level (<10 ng/ml vs. ≥10 ng/ml) at baseline are shown in Table 1. Patients with elevated AFP (≥10 ng/ml) were characterized by older age ($P < 0.001$), high ALT level ($P < 0.001$), low platelet count ($P < 0.001$), low albumin level ($P < 0.001$), and progression of hepatic inflammation ($P < 0.001$) and fibrosis ($P < 0.001$). No significant difference was seen in gender, HCV genotype, or HCV-RNA viral load. Multivariate logistic regression analysis revealed that the factors correlated with elevated serum AFP at baseline were low serum albumin level ($P = 0.001$) and severe hepatic inflammation ($P = 0.02$) (Table 2).

Changes in Serum AFP Level During and After IFN Therapy

Mean duration of IFN therapy was 39.6 ± 16.5 weeks. One hundred thirty-two (50.2%) patients were treated for 24 to 47 weeks, and 131 (49.8%) were treated for 48 or more weeks. Of the 263 patients treated with IFNs, 136 (51.7%) were defined as SVR, 51 (19.4%) as relapse, and 76 (28.9%) as NR. Serum AFP levels decreased gradually during IFN therapy without fluctuations, and a significant decrease was observed regardless of response to treatment. ($P < 0.001$, $P = 0.003$, and $P < 0.001$ for SVR, relapse, and NR, respectively). In the SVR group, a decrease in serum AFP level was also observed after treatment ($P = 0.037$) (Table 3). The significant decrease of serum AFP level was not associated with hepatic fibrosis, as seen in both patients with mild (F0-2) ($P < 0.001$) and severe hepatic fibrosis (F3 and F4) ($P = 0.012$) (Table 4).

Next, we evaluated the changes in serum AFP level according to the treatment regimens. Among patients treated with Peg-IFNα-2b, recombinant IFNα-2b and Peg-IFNα-2a, the decrease in the serum AFP level during IFN therapy was not associated with the treatment regimen ($P < 0.001$, $P < 0.001$ and $P = 0.001$, for Peg-IFNα-2b

Table 1 Clinical features of patients classified by serum AFP level at baseline

Characteristics	AFP <10 ng/ml ($n = 191$)	AFP ≥10 ng/ml ($n = 72$)	*P*-value
Age (years)	54.3 ± 11.8	60.0 ± 8.6	<0.001
Gender (Female/Male)	84/107	41/31	0.072
ALT (IU/l)	85.8 ± 88.1	104.5 ± 66.3	<0.001
Platelet ($\times 10^4/\mu l$)	16.8 ± 5.6	13.1 ± 4.8	<0.001
Albumin (g/dl)	4.4 ± 0.3	4.0 ± 0.5	<0.001
Histopathology			
Inflammation (A0-1/A2-3)	68/57	7/42	<0.001
Fibrosis (F0-2/F3-4)	116/9	30/19	<0.001
HCV-RNA			
Serology (Group 1/2)	131/57	54/18	0.446
Viral load (0-99/100-499/500 < KIU/ml)	18/39/99	8/16/30	0.588

ALT alanine aminotransferase, *AFP* alpha-fetoprotein, *HCV* hepatitis C virus. Values are expressed as mean ± SD

Table 2 Multivariate logistic regression analysis for predicting elevated AFP (≥10 ng/ml) at baseline

Variables	Coefficient	SE	OR (95% CI)	*P*-value
Albumin (g/dl)	−2.502	0.724	0.082 (0.020–0.339)	0.001
Inflammation (A0-1/A2-3)	1.525	0.656	4.594 (1.270–16.617)	0.020

SE standard error, *OR* odds ratio, *CI* confidence interval

Table 3 Changes in serum AFP level during and after IFN therapy according to the virologic response

Virological response	Baseline	EOT	24 weeks after EOT
SVR			
Median AFP (ng/ml)	4.2	3.4*	3.3†
(range)	(1.0–153.0)	(1.0–12.9)	(1.0–10.3)
Relapse			
Median AFP (ng/ml)	5.8	4.1**	3.9
(range)	(1.0–271.8)	(2.0–31.6)	(1.0–82.7)
NR			
Median AFP (ng/ml)	8.3	5.9*	6.0
(range)	(1.5–542.0)	(1.5–59.8)	(1.3–109.0)

Wilcoxon signed-ranks test was used. * $P < 0.001$, compared to baseline; ** $P = 0.003$, compared to baseline; † $P = 0.037$, compared to EOT

AFP alpha-fetoprotein, *SVR* sustained virologic response, *NR* non-response, *EOT* end of treatment

Table 4 Changes in serum AFP level during and after IFN therapy according to the hepatic fibrosis

Hepatic fibrosis	Baseline	EOT	24 weeks after EOT
Slight fibrosis, F0-2			
Median AFP (ng/ml)	4.4	3.5*	3.3
(range)	(1.0–153.0)	(1.0–59.8)	(1.0–37.4)
Advanced fibrosis, F3-4			
Median AFP (ng/ml)	14.1	6.5**	6.3
(range)	(2.6–542.0)	(1.5–54.4)	(1.8–82.7)

Wilcoxon signed-ranks test was used. * $P < 0.001$, compared to baseline; ** $P = 0.012$, compared to baseline

AFP alpha-fetoprotein, *EOT* end of treatment

and ribavirin, recombinant IFNα-2b and ribavirin, Peg-IFNα-2a, respectively) (Table 5). We were unable to evaluate the changes in serum AFP level in patients treated with consensus IFNα or natural IFNα owing to the small number of cases.

Risk Factors for Development of HCC

The mean observation period from initiation of IFN therapy was 162.4 ± 82.3 weeks (range, 89.7–367.7). HCC developed in seven patients within the study period. The final diagnosis of HCC was determined by imaging modalities. Two of the seven were patients defined as SVR and five as NR. The mean length of time from initiation of IFN therapy to diagnosis of HCC was 129.0 ± 77.3 weeks. Serum AFP levels at diagnosis of HCC were 2.2, 3.0, 4.0, 10.9, 11.9, 17.4, and 47.0 ng/ml. Of these seven patients, one showed F3 fibrosis, two were diagnosed clinically as having cirrhosis, and the other four were diagnosed as having chronic hepatitis at the start of IFN treatment. In the follow-up period from EOT to diagnosis of HCC, a pattern of AFP increase, a stable AFP pattern and a pattern of AFP decrease were seen in three, three and one patients, respectively (data not shown). Table 6 represents the changes in serum AFP level during and after IFN therapy in the patients who developed HCC and in those who did not. Univariate Cox's regression analysis revealed that older age at the initiation of therapy ($P = 0.038$) was a significant prognostic indicator of the development of HCC after IFN therapy, and increased serum AFP levels at EOT ($P = 0.057$) was a close-to-significant variable (Table 7). We examined the cumulative incidence of HCC development on the basis of serum AFP level (<10 ng/ml vs. ≥10 ng/ml) at EOT (Fig. 1). Patients with AFP ≥10 ng/ml had a significantly higher incidence of HCC than did those with AFP <10 ng/ml by log-rank test ($P = 0.021$).

Table 5 Changes in serum AFP level during and after IFN therapy according to the treatment regimens

Treatment regimens	Baseline	EOT	24 weeks after EOT
Peg-IFN α-2b + RBV			
Median AFP (ng/ml)	5.0	3.9*	4.0
(range)	(1.4–77.8)	(1.5–22.2)	(1.4–26.3)
Rec-IFN α-2b + RBV			
Median AFP (ng/ml)	7.3	4.1*	4.0
(range)	(1.0–542.0)	(1.0–54.4)	(1.0–35.1)
Peg-IFN α-2a			
Median AFP (ng/ml)	4.0	3.8**	3.5
(range)	(1.0–271.8)	(1.5–31.6)	(1.0–82.7)

Wilcoxon signed-ranks test was used. * $P < 0.001$, compared to baseline; ** $P = 0.001$, compared to baseline

AFP alpha-fetoprotein, *Peg-IFN* pegylated-IFN, *Rec-IFN* recombinant IFN, *RBV* Ribavirin, *EOT* end of treatment

Table 6 Changes in serum AFP level during and after IFN therapy in those with patients who developed HCC and in those without HCC

Patients	Baseline	EOT	24 weeks after EOT
Patients developed HCC			
Median AFP (ng/ml)	8.5	17.9	7.6
(range)	(3.6–61.0)	(2.2–46.0)	(1.0–109.0)
Patients without HCC			
Median AFP (ng/ml)	5.1	3.9*	3.9
(range)	(1.0–542.0)	(1.5–59.8)	(1.0–82.7)

Wilcoxon signed-ranks test was used. * $P < 0.001$, compared to baseline

AFP alpha-fetoprotein, *EOT* end of treatment

Table 7 Factors associated with the development of HCC after IFN therapy by univariate Cox's regression analysis

Variables	HR (95% CI)	*P*-value
Pre-treatment baseline variables		
Age (years)	1.117 (1.006–1.239)	0.038
Gender (Female/Male)	1.888 (0.365–9.772)	0.449
ALT (IU/l)	0.996 (0.984–1.009)	0.570
AFP (ng/ml)	0.998 (0.980–1.017)	0.856
Platelet ($\times 10^4/\mu l$)	0.956 (0.830–1.102)	0.539
Albumin (g/dl)	1.569 (0.159–15.518)	0.700
Histopathology		
Inflammation (A0-1/A2-3)	0.624 (0.086–4.521)	0.641
Fibrosis (F0-2/F3-4)	1.362 (0.137–13.558)	0.792
HCV-RNA		
Serology (Group 1/2)	1.195 (0.231–6.187)	0.832
Viral load (0-99/100-499/500 < KIU/ml)	1.422 (0.346–5.849)	0.625
Duration of therapy (week)	0.997 (0.919–1.038)	0.453
Efficacy of IFN (SVR/Relapse/NR)	2.453 (0.476–12.652)	0.284
Post-treatment variables at EOT		
ALT (IU/l)	1.006 (0.998–1.014)	0.137
AFP (ng/ml)	1.048 (0.999–1.101)	0.057
Platelet ($\times 10^4/\mu l$)	1.020 (0.889–1.171)	0.777
Albumin (g/dl)	0.115 (0.005–2.776)	0.183

HR hazard ratio, *CI* confidence interval, *ALT* alanine aminotransferase, *AFP* alpha-fetoprotein, *HCV* hepatitis C virus, *SVR* sustained virologic response, *NR* non-response, *EOT* end of treatment

Discussion

Until now, there has been little information on the relationship between the changes in serum AFP level associated with IFN therapy and the development of HCC, although several reports have described the changes in serum AFP level during IFN therapy. Consistent with our results, Murashima et al. [21] have already reported that IFN reduces the serum AFP level during treatment regardless of virologic response. Nomura et al. [23] also showed a significant decrease in serum AFP level during low-dose and long-term IFN monotherapy in 44 aged patients with CHC; SVR status was achieved in only two. In contrast, Chen et al. [22] demonstrated a significant decrease in serum AFP level during and after IFN therapy in an SVR group ($n = 26$), whereas no significant decrease in serum AFP level was observed in the non-SVR group ($n = 9$). The association of changes in serum AFP level during IFN therapy with the development of HCC was not examined in these studies.

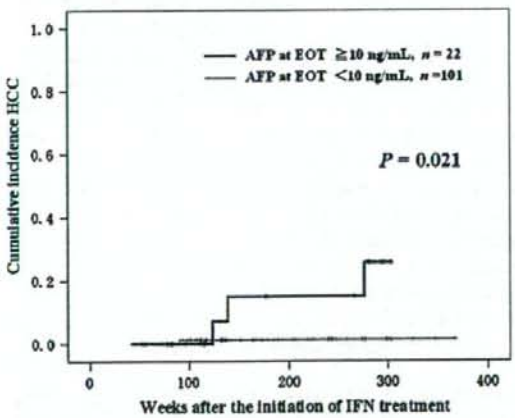

Fig. 1 Cumulative incidence HCC in two groups (serum AFP level <10 ng/ml, $n = 101$; vs. ≥10 ng/ml, $n = 22$) at the end of treatment. The high AFP group had a significantly higher incidence of HCC ($P = 0.021$). *AFP* alpha-fetoprotein, *EOT* end of treatment

We demonstrated that the serum AFP level in patients with CHC decreased during IFN therapy regardless of virologic response, and that, by univariate Cox's regression analysis, AFP level at EOT was a close-to-significant prognostic factor affecting the development of HCC. Moreover, a significantly higher cumulative incidence of HCC was seen in patients with increased serum AFP levels at EOT by log-rank test. Our results suggest that serum AFP level at EOT is a possible predictor of HCC development after IFN therapy and will be useful for considering additional treatments, such as long-term administration of low-dose IFN, to prevent HCC development.

AFP is a fetal glycoprotein produced by the yolk sac and fetal liver. Following birth, AFP is replaced by albumin as the major serum protein, and then the AFP level decreases rapidly. Consequently, AFP is not detectable in the sera of adults. However, production of AFP in adults occurs during liver regeneration and hepatocarcinogenesis. Therefore,

AFP has been used as a diagnostic marker for HCC [14, 15], although AFP levels are sometimes elevated in patients with chronic hepatitis and cirrhosis who have no evidence of HCC [16–18]. The reported prevalence of elevated AFP in patients with CHC varies from 10 to 43% [18, 19, 26, 27]. This wide discrepancy among previous reports is probably due to differences in the definition of elevated AFP value, as well as in patient population, ethnicity, and sample size. Chu et al. [18] reported that 28.7% (33/115) of patients with CHC had an elevated serum AFP level (≥12 ng/ml). Chen et al. [22] also reported that an elevated AFP level (≥10 ng/ml) was seen in 33% (41/123) of patients with CHC. Our results revealed that 27.0% (72/263) of patients with CHC had an elevated serum AFP level (≥10 ng/ml). This result is consistent with those of previous reports from Asian countries [18, 22].

Our multivariate logistic regression analysis revealed that hepatic inflammation and serum albumin level were significant independent factors associated with serum AFP level at baseline. Consistent with our results, several reports have shown that serum AFP level is correlated with the degree of hepatic inflammation in liver biopsy specimens [20]. Moreover, a number of studies have shown a relationship between elevated serum AFP level and decreased serum albumin level in patients with CHC [18, 21]. One of the reasons for these associations is simply the fact that advanced liver damage results in decreased production of albumin. In addition, reciprocal changes in albumin and AFP gene transcription during liver regeneration may account for the relationship between elevated serum AFP level and decreased serum albumin level [28, 29]. Although advanced hepatic fibrosis has been reported as the most common cause of serum AFP elevation [18, 22], our multivariate analysis was unable to demonstrate any association between serum AFP level and advanced hepatic fibrosis. In the present study, however, stage 3–4 fibrosis was significantly more frequent in the group showing elevated serum AFP levels. Moreover, the association of an elevated AFP level with a low albumin level may be secondary to a decrease of liver synthetic function due to cirrhosis. We speculated that one of the reasons for the discrepancy might be the fact that only 49 patients with an elevated serum AFP level underwent liver biopsy.

Many reports have described elevated serum AFP level, together with age, gender, and liver histologic stage, as independent risk factors for HCC in patients with CHC [4, 5]. Our results revealed that the hepatic inflammation was a significant independent factor associated with serum AFP level at baseline. These results indicate that active inflammation in the liver is one of the most important factors influencing serum AFP level, and suggest that this persistent inflammation results in hepatocarcinogenesis. In contrast, a number of reports have revealed that AFP itself can enhance the proliferation of mammalian tumor cells. Wang and Xu et al. [30] have reported that human AFP increases the proliferation of mouse H-22 hepatoma cells, and that the growth stimulatory activity of AFP could be abolished by anti-AFP antibodies. Wang and Xie et al. [31] showed that AFP enhances the proliferation of human HCC cells, and they suggested that this effect was mediated by an AFP/receptor autocrine pathway. In addition, AFP stimulates the expression of some oncogenes in human HCC cells and has immunosuppressive activity [32, 33]. These results suggest that not only hepatic inflammation accompanied by elevation of serum AFP level, but AFP itself, is associated with hepatocarcinogenesis.

Our univariate Cox's regression analysis revealed that serum AFP level at EOT was a close-to-significant prognostic variable affecting the development of HCC, although serum AFP level before treatment was not. Consistent with these results, Arase et al. [24] reported that in patients with CHC who were treated with IFN or herbal medicine, elevated serum AFP level (>10 ng/ml) after treatment was a statistically significant independent prognostic factor in the development of HCC. There are some factors other than AFP that could have a potential association with the development of HCC. Several studies have implicated obesity, diabetes, intake of alcohol, and smoking, as risk factors for HCC [34–37]. However, we did not investigate these factors in the present retrospective study. In addition, we were unable to exclude the possibility of occult HBV infection in patients with HCC, although all patients were negative for HBsAg.

In conclusion, our results revealed that serum AFP level decreased during IFN therapy regardless of the virologic response. In addition, serum AFP level at EOT was a close-to-significant prognostic factor for HCC development. These results suggest that serum AFP level at EOT should be utilized in making decisions on additional therapeutic options, such as long-term administration of low-dose IFN, to reduce the risk of HCC development in patients in whom HCV elimination by routine IFN therapy has failed. We realize our study has some limitations as follows: first, it was a retrospective analysis; second, various kinds of IFN were used; and third, the duration of IFN therapy varied from 24 to 90 weeks. Further prospective studies in which patients are treated by the current standard protocol-Peg-IFN with ribavirin-for a set period of time will confirm the relationship between changes in serum AFP level associated with IFN therapy and the development of HCC.

Acknowledgments The following doctors at each of the institutions participating in the Niigata Liver Disease Study Group contributed equally to the study: Nobuo Waguri and Kentaro Igarashi (Niigata City General Hospital, Niigata), Toru Ishikawa and Tomoteru Kamimura (Saiseikai Niigata Second Hospital, Niigata), Motoya Sugiyama (Niigata Prefectural Shibata Hospital, Shibata), Soichi Sugitani

(Tachikawa General Hospital, Nagaoka), Norio Ogata (Tsubame Rosai Hospital, Tsubame), Toru Hatano (Nagaoka Chuo General Hospital, Nagaoka), Toru Takahashi (Nagaoka Red Cross Hospital, Nagaoka), Hitoshi Bannai (Saiseikai Sanjo Hospital, Sanjo), Hiroto Wakabayashi (Takeda General Hospital, Aizuwakamatsu), Atsuo Sekine (Niigata Prefectural Yoshida Hospital, Tsubame), Toshiyuki Kato (Niigata Prefectural Cancer Center Hospital, Niigata), Masaaki Hirano (Niigata Prefectural Central Hospital, Joetsu), and Toru Miyajima (Toyosaka Hospital, Niigata).

References

1. Bruix J, Barrera JM, Calvet X, et al. Prevalence of antibodies to hepatitis C virus in Spanish patients with hepatocellular carcinoma and hepatic cirrhosis. *Lancet*. 1989;334:1004–1046. doi: 10.1016/S0140-6736(89)91015-5.
2. Colombo M, Kuo G, Choo QL, et al. Prevalence of antibodies to hepatitis C virus in Italian patients with hepatocellular carcinoma. *Lancet*. 1989;334:1006–1008. doi:10.1016/S0140-6736(89)91016-7.
3. Hasan F, Jeffers LJ, De Medina M, et al. Hepatitis C-associated hepatocellular carcinoma. *Hepatology*. 1990;12:589–591. doi: 10.1002/hep.1840120323.
4. Ikeda K, Saitoh S, Koida I, et al. A multivariate analysis of risk factors for hepatocellular carcinogenesis: a prospective observation of 795 patients with viral and alcoholic cirrhosis. *Hepatology*. 1993;18:47–53.
5. Tsukuma H, Hiyama T, Tanaka S, et al. Risk factors for hepatocellular carcinoma among patients with chronic liver disease. *N Engl J Med*. 1993;328:1797–1801. doi:10.1056/NEJM199306243282501.
6. Davis GL, Balart LA, Schiff ER, et al. Treatment of chronic hepatitis C with recombinant interferon alfa. A multicenter randomized, controlled trial. Hepatitis Interventional Therapy Group. *N Engl J Med*. 1989;321:1501–1506.
7. Di Bisceglie AM, Martin P, Kassianides C, et al. Recombinant interferon alfa therapy for chronic hepatitis C. A randomized, double-blind, placebo-controlled trial. *N Engl J Med*. 1989;321:1506–1510.
8. Causse X, Godinot H, Chevallier M, et al. Comparison of 1 or 3 MU of interferon alfa-2b and placebo in patients with chronic non-A, non-B hepatitis. *Gastroenterology*. 1991;101:497–502.
9. Chayama K, Saitoh S, Arase Y, et al. Effect of interferon administration on serum hepatitis C virus RNA in patients with chronic hepatitis C. *Hepatology*. 1991;13:1040–1043.
10. Nishiguchi S, Kuroki T, Nakatani S, et al. Randomised trial of effects of interferon-alpha on incidence of hepatocellular carcinoma in chronic active hepatitis C with cirrhosis. *Lancet*. 1995;346:1051–1055. doi:10.1016/S0140-6736(95)91739-X.
11. Ikeda K, Saitoh S, Arase Y, et al. Effect of interferon therapy on hepatocellular carcinogenesis in patients with chronic hepatitis type C: a long-term observation study of 1, 643 patients using statistical bias correction with proportional hazard analysis. *Hepatology*. 1999;29:1124–1130. doi:10.1002/hep.510290439.
12. Makiyama A, Itoh Y, Kasahara A, et al. Characteristics of patients with chronic hepatitis C who develop hepatocellular carcinoma after a sustained response to interferon therapy. *Cancer*. 2004;101:1616–1622. doi:10.1002/cncr.20537.
13. Ikeda M, Fujiyama S, Tanaka M, et al. Risk factors for development of hepatocellular carcinoma in patients with chronic hepatitis C after sustained response to interferon. *J Gastroenterol*. 2005;40:148–156. doi:10.1007/s00535-004-1519-2.
14. Abelev GI. Production of embryonal serum alpha-globulin by hepatoma: review of experimental and clinical data. *Cancer Res*. 1968;28:1344–1350.
15. Conor GI, Tatarinov YS, Abelev GI, Uriel J. A collaborative study for the evaluation of a serologic test for primary liver cancer. *Cancer*. 1970;25:1091–1098. doi:10.1002/1097-0142(197005)25:5<1091::AID-CNCR2820250514>3.0.CO;2-P.
16. Bayati N, Silverman AL, Gordon SC. Serum alpha-fetoprotein levels and liver histology in patients with chronic hepatitis C. *Am J Gastroenterol*. 1998;93:2452–2456. doi:10.1111/j.1572-0241.1998.00703.x.
17. Goldstein NS, Blue DE, Hankin R, et al. Serum alpha-fetoprotein levels in patients with chronic hepatitis C. Relationships with serum alanine aminotransferase values, histologic activity index, and hepatocyte MIB-1 scores. *Am J Clin Pathol*. 1999;111:811–816.
18. Chu CW, Hwang SJ, Luo JC, et al. Clinical, virologic, and pathologic significance of elevated serum alpha-fetoprotein levels in patients with chronic hepatitis C. *J Clin Gastroenterol*. 2001;32:240–244. doi:10.1097/00004836-200103000-00014.
19. Hu KQ, Kyulo NL, Lim N, Elhazin B, Hillebrand DJ, Bock T. Clinical significance of elevated alpha-fetoprotein (AFP) in patients with chronic hepatitis C, but not hepatocellular carcinoma. *Am J Gastroenterol*. 2004;99:860–865. doi:10.1111/j.1572-0241.2004.04152.x.
20. Di Bisceglie AM, Sterling RK, Chung RT, et al. HALT-C Trial group: serum alpha-fetoprotein levels in patients with advanced hepatitis C: results from the HALT-C Trial. *J Hepatol*. 2005;43:434–441. doi:10.1016/j.jhep.2005.03.019.
21. Murashima S, Tanaka M, Haramaki M, et al. A decrease in AFP level related to administration of interferon in patients with chronic hepatitis C and a high level of AFP. *Dig Dis Sci*. 2006;51:808–812. doi:10.1007/s10620-006-3211-2.
22. Chen TM, Huang PT, Tsai MH, et al. Predictors of alpha-fetoprotein elevation in patients with chronic hepatitis C, but not hepatocellular carcinoma, and its normalization after pegylated interferon alfa 2a-ribavirin combination therapy. *J Gastroenterol Hepatol*. 2007;22:669–675.
23. Nomura H, Kashiwagi Y, Hirano R, et al. Efficacy of low-dose long-term interferon monotherapy in aged patients with chronic hepatitis C genotype 1 and its relation to alpha-fetoprotein: a pilot study. *Hepatol Res*. 2007;37:490–497. doi:10.1111/j.1872-034X.2007.00073.x.
24. Arase Y, Suzuki F, Suzuki Y, et al. Prolonged-efficacy of bisphosphonate in postmenopausal women with osteoporosis and chronic liver disease. *J Med Virol*. 2008;80:1302–1307. doi: 10.1002/jmv.21195.
25. Ichida F, Tsuji T, Omata M, et al. New Inuyama Classification; new criteria for histological assessment of chronic hepatitis. *Int Hepatol Commun*. 1996;6:112–119. doi:10.1016/S0928-4346(96)00325-8.
26. Fattovich G, Giustina G, Degos F, et al. Morbidity and mortality in compensated cirrhosis type C: a retrospective follow-up study of 384 patients. *Gastroenterology*. 1997;112:463–472. doi:10.1053/gast.1997.v112.pm9024300.
27. Sato Y, Nakata K, Kato Y, et al. Early recognition of hepatocellular carcinoma based on altered profiles of alpha-fetoprotein. *N Engl J Med*. 1993;328:1802–1806. doi:10.1056/NEJM199306243282502.
28. Niwa Y, Matsumura M, Shiratori Y, et al. Quantitation of alpha-fetoprotein and albumin messenger RNA in human hepatocellular carcinoma. *Hepatology*. 1996;23:1384–1392.
29. Panduro A, Shalaby F, Weiner FR, Biempica L, Zern MA, Shafritz DA. Transcriptional switch from albumin to alpha-fetoprotein and changes in transcription of other genes during carbon tetrachloride induced liver regeneration. *Biochemistry*. 1986;25:1414–1420. doi:10.1021/bi00354a034.
30. Wang XW, Xu B. Stimulation of tumor-cell growth by alpha-fetoprotein. *Int J Cancer*. 1998;75:596–599. doi:10.1002/(SICI)1097-0215(19980209)75:4<596::AID-IJC17>3.0.CO;2-7.

31. Wang XW, Xie H. Alpha-fetoprotein enhances the proliferation of human hepatoma cells in vitro. *Life Sci*. 1999;64:17–23. doi: 10.1016/S0024-3205(98)00529-3.
32. Li MS, Li PF, Chen Q, Du GG, Li G. Alpha-fetoprotein stimulated the expression of some oncogenes in human hepatocellular carcinoma Bel 7402 cells. *World J Gastroenterol*. 2004;10: 819–824.
33. Li MS, Ma QL, Chen Q, et al. Alpha-fetoprotein triggers hepatoma cells escaping from immune surveillance through altering the expression of Fas/FasL and tumor necrosis factor related apoptosis-inducing ligand and its receptor of lymphocytes and liver cancer cells. *World J Gastroenterol*. 2005;11:2564–2569.
34. Chen CL, Yang HI, Yang WS, et al. Metabolic factors and risk of hepatocellular carcinoma by chronic hepatitis B/C infection: a follow-up study in Taiwan. *Gastroenterology*. 2008;135:111–121. doi:10.1053/j.gastro.2008.03.073.
35. Hassan MM, Hwang LY, Hatten CJ, et al. Risk factors for hepatocellular carcinoma: synergism of alcohol with viral hepatitis and diabetes mellitus. *Hepatology*. 2002;36:1206–1213. doi: 10.1053/jhep.2002.36780.
36. Yuan JM, Govindarajan S, Arakawa K, Yu MC. Synergism of alcohol, diabetes, and viral hepatitis on the risk of hepatocellular carcinoma in blacks and whites in the US. *Cancer*. 2004;101: 1009–1017. doi:10.1002/cncr.20427.
37. Chiba T, Matsuzaki Y, Abei M, et al. The role of previous hepatitis B virus infection and heavy smoking in hepatitis C virus-related hepatocellular carcinoma. *Am J Gastroenterol*. 1996;91: 1195–1203.

Optical Microscopic Findings of the Behavior of Perflubutane Microbubbles Outside and Inside Kupffer Cells During Diagnostic Ultrasound Examination

Guang-jian Liu, MD,† Fuminori Moriyasu, MD, PhD,* Tomihiko Hirokawa, MD, PhD,* Munire Rexiati, MD,* Masahiko Yamada, MD, PhD,* and Yasuharu Imai, MD, PhD**

Purpose: To investigate the behavior of perflubutane microbubbles outside and inside Kupffer cells during diagnostic ultrasound (US) examination, and to determine the thresholds of the acoustic pressure of different kinds of behavior.

Methods: Acoustic behavior of perflubutane microbubbles inside and outside Kupffer cells in an acoustic field induced by a clinical US transducer and equipment was optically observed in vitro. The acoustic pressure was measured simultaneously by a calibrated hydrophone and an oscilloscope.

Results: The acoustic behavior of microbubbles was optically categorized as stabilization, oscillation, transposition, shrinkage, and destruction. The mechanical index (MI) displayed on the US equipment correlated well with the acoustic pressure at the level of microbubbles measured hydrophonically. At a frame rate of 15 Hz with a frequency of 3.5 MHz and pulse repetition frequency of 3 KHz, the thresholds in term of MI for free microbubbles to begin oscillation, reach best oscillation, transposition, shrinkage, and destruction were 0.21, 0.44, 0.53, 0.75, and 1.03, respectively. Although adherent and phagocytosed microbubbles showed more stability enduring insonation compared with free microbubbles, the thresholds of shrinkage and destruction were MI 1.03 and 1.18 for adherent microbubbles, and 1.18 and 1.37 for phagocytosed microbubbles, respectively. Neither oscillation nor transposition of microbubbles inside Kupffer cells was observed microscopically. No cell damage because of microbubbles destruction was found in the present study.

Conclusion: Perflubutane microbubbles outside and inside Kupffer cells respond to external US insonation with same parameters of a clinical contrast-enhanced US study according to the acoustic pressure. Free microbubbles behave as stabilization, oscillation, transposition, shrinkage, and destruction under insonation. The adherent and phagocytosed microbubbles are more stable under insonation than free microbubbles, but still respond showing shrinkage and destruction when MI is over 1.03.

Key Words: behavior, Kupffer cells, microbubbles, ultrasound

(*Invest Radiol* 2008;43: 829–836)

Perflubutane microbubbles (Sonazoid, Amersham Health, Oslo, Norway) have been proved to be phagocytosed by Kupffer cells in both in vitro and in vivo studies.[1,2] The microbubbles inside the reticuloendothelial cells partly contribute to the delayed phase images of contrast-enhanced ultrasound (CEUS).[1–3] The interactions between the acoustic field and microbubble contrast agent are critical for the CEUS imaging process. CEUS imaging is generally based on the cancellation and/or separation of linear ultrasound (US) signals from tissue and utilization of the nonlinear response from microbubbles which originated from microbubble oscillation at low acoustic pressure and/or microbubble disruption at high acoustic pressure.[4–6] To understand the acoustic behavior of microbubbles and its correlation with the mechanical index (MI), displayed on the US scanner, is critical to optimize the setting of the contrast-specific imaging in clinical work.

Apart from the use of microbubble US contrast agent in diagnostic US imaging,[6–8] more advanced applications of microbubbles such as molecular imaging, drug and gene delivery, and the direct stimulation of therapeutic arteriogenesis are showing great potential on an effective and less invasive method for both diagnosis and treatment in the future.[9–17] To understand the acoustic behavior of adherent and phagocytosed microbubbles is very important to improve the efficiency of drug or gene transduction and treatment.

This article reported our preliminary study of in vitro optical observation of the acoustic behavior of perflubutane microbubbles both outside and inside Kupffer cells, and the thresholds of acoustic pressure associated with different kinds of behavior using clinically used US equipment.

MATERIALS AND METHODS

Kupffer Cell Isolation and Culture

Male Wistar rats aged 12 to 16 weeks and weighing 200 g to 400 g were used for isolation of Kupffer cells in this

Received April 15, 2008, and accepted for publication, after revision, June 28, 2008.

From the *Department of Gastroenterology and Hepatology, Tokyo Medical University, Nishi-Shinjuku, Shinjuku-ku, Tokyo; and †Department of Medical Ultrasound, Institute of Diagnostic and Interventional Ultrasound, The First Affiliated Hospital of Sun Yat-Sen University, Guangzhou, People's Republic of China.

Reprints: Fuminori Moriyasu, MD, PhD, Department of Gastroenterology and Hepatology, Tokyo Medical University, 6-7-1 Nishi-Shinjuku, Shinjuku-ku, Tokyo 160-0023. E-mail: moriyasu@tokyo-med.ac.jp.

ISSN: 0020-9996/08/4312-0829

study (CLEA Japan Inc., Tokyo, Japan). Intraperitoneal injection of pentobarbital sodium (50 mg/kg, Dainippon Sumitomo Pharma Co., Ltd., Osaka, Japan) was used for anesthesia in all animals. After successful cannulation of the portal vein and inferior vena cava, the liver was perfused in situ by order of calcium-free minimum essential medium (Sigma-Aldrich, Inc., St. Louis, MI), 0.3% pronase (Roche Diagnostics Corp., Indianapolis, IN), and 0.025% type IV collagenase (Sigma) in Dulbecco modified Eagle medium/F-12 (Sigma). Then liver was removed and minced by scissors, and digested in 0.035% pronase and 62.5 U/mL DNase (Sigma) in Dulbecco modified Eagle medium/F-12 within a shaker at 37°C for 20 minutes. After filtration through gauze and several centrifugations, the cells were harvested in RPMI 1640 cell culture medium (Sigma) with 10% fetal bovine serum (ICN Biomedical Inc. Aurora, OH), and seeded onto small glass plates that had been fixed onto specially made frames with 4 mm in total thickness. After a 2-hour incubation at 37°C in 10-cm culture dishes, the glass plates were washed with Hanks balanced salt solution (Sigma) to remove the unattached cells. Finally, Kupffer cells were cultured in RPMI 1640 supplemented with 10% fetal bovine serum and 100 U/mL penicillin (Invitrogen, Carlsbad, CA) at 37°C in a humidified atmosphere containing 5% CO_2 and air for 24 hours before the experiment. The methods for Kupffer cell isolation and culture have been described in detail previously.[1] The purity of the isolated Kupffer cells was over 96%, tested by the uptake of 2-μm latex beads (Polyscience, Warrington, PA),[18] and their viability was over 90% on the trypan-blue dye exclusion test. All animals were treated with humanity during the whole experiment. The experimental protocols were approved by the animal ethical committee of Tokyo Medical University.

Contrast Agent Preparation

Sonazoid (Daiichi Sankyo Company, Ltd., Tokyo, Japan) was used in this study. The freeze-dried agent in vials was mixed with 2 mL of distilled water and shaken until completely dispersed according to the manufacture's instruction. Further dilution was made by adding 0.02 mL of original Sonazoid solution into 19.98 mL distilled water to adjust to 1/1000 of the standard concentration of the contrast agent. The final concentration of microbubbles used for the in vitro study was about 1×10^6/mL.[19]

Phagocytosis of Microbubbles by Kupffer Cells

The small glass plates on which Kupffer cells had been cultured were turned upside down, and moved into new culture dishes with 40 mL RPMI 1640 cell culture medium. A contrast agent (0.5 mL) of 1/1000 standard concentration was added under the small glass plates through a curved 21 G needle. The phagocytic process of microbubbles was observed for at least 30 minutes under inverted culture tissue microscope (IX71, Olympus, Tokyo, Japan) equipped with a heater microscope stage (MPF-10-O, IEDA Trading Corp., Japan) to maintain the culture medium at 37°C. The whole process was recorded on a digital video cassette recorder (DSR-20MD, Sony, Tokyo, Japan) through a 3CCD camera (JU-TU531T, Toshiba Corp., Tokyo, Japan) attached to the microscope.

TABLE 1. Setting of Ultrasound Scanner Used in the Experiment

Parameter	Specification/Setting
Machine type	Toshiba Aplio XG with PVT 382BT probe
Imaging mode	Pulse inversion imaging
MI	0.08 to 1.6 (as read on screen)
Frequency (MHz)	3.5
Pulse repetition frequency (PRF) (KHz)	3–5
Frame rate (Hz)	1 or 15
Depth (cm)	4
Focus position (cm)	4
Focus number	1

US Exposure

A clinical US scanner (Toshiba Aplio XG, Toshiba Corp., Tokyo, Japan) and a microconvex probe with a frequency range of 1 to 6 MHz (PVT 382BT, Toshiba Corp.) were used in the present experiment. Pulse inversion imaging mode was used for all experiments (Table 1). The probe was fixed onto a stable mechanical arm, and its surface was immersed into the culture medium with the microscope stage at an angle of 45 degree. The setup for US exposure is shown in Figure 1. US exposure lasted for 10 seconds each time and MI was increased from 0.08 to 1.6, gradually. To tell the difference of US exposure duration to microbubbles' behavior, both high frame rate (15 Hz) and low frame rate (1 Hz) US exposure were studied. Four dishes of Kupffer cells were used for observation under high frame rate US insonation and 2 dishes for the low frame rate study. The whole process of US exposure was recorded by the same video system as previously described.

Measurement of Acoustic Pressure

A calibrated needle hydrophone (Müller-Platte, Bensheim, Germany) and a digital storage oscilloscope (Agilent 3102A, Colorado) were used to measure the acoustic pressure. The setup for acoustic pressure measurement is shown

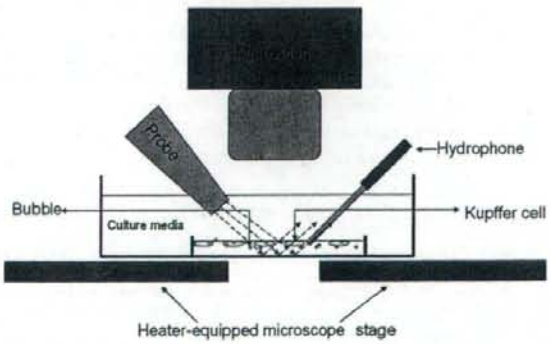

FIGURE 1. Scheme of the experimental setup. The ultrasound probe and the hydrophone were fixed at 45 degree to the microscope stage. The dotted line represents the propagation of ultrasound waves.

in Figure 1. The head of needle hydrophone was fixed at the same level of Kupffer cells and microbubbles through a small man-made hole on the glass plate with the microscope stage at an angle of 45 degree. The pressure range was read by the oscilloscope during the US exposure under a certain MI.

Data Analysis and Statistics

The videos of the phagocytic process of microbubbles and behavior of microbubbles under US exposure were simultaneously reviewed by 2 researchers who were blinded to the experiment, and the decision was made on consensus. The microbubbles in the field of vision were divided into 3 types as free microbubbles, adherent microbubbles, and phagocytosed microbubbles. Free microbubbles were those who float freely in the media and have no contact with the Kupffer cells; adherent microbubbles were defined as microbubbles that have adhered to the membrane of Kupffer cells but were still outside the cells; and phagocytosed microbubbles were those that have been inside the Kupffer cells.

The microbubbles showed 5 different types of acoustic behavior under optical microscope observation which were described as stabilization, oscillation, transposition, shrinkage, and destruction. Stabilization was defined as microbubbles so significantly stable that observers cannot tell any movement under optical microscope; oscillation was defined as slight microbubble vibration in situ; transposition referred to microbubbles shaking violently and rapidly; shrinkage was obvious decrease in size of the microbubbles; and destruction was defined as immediate disappearance of the microbubbles.

The numbers of different types of microbubbles showing different kinds of behavior were counted using slow speed replay of the videotapes combined with still images from videotapes. The ratios of different types of microbubbles with different behavior under certain US exposure were expressed as the number of microbubbles with a given behavior against the total number of the same type of microbubbles in a single field.

Cell damage was defined as rupture of cell membrane and leakage of cytoplasm content under optical microscopic observation. The difference of cell damage after US exposure between the high and low frame rate US insonation was compared using Fisher exact test. A value of $P < 0.05$ was considered statistically significant. The statistical analyses and graphs were performed using the SPSS 10.0 software package (SPSS Inc., Chicago, IL).

RESULTS

Phagocytosis of Microbubbles by Kupffer Cells

Over 90% of Kupffer cells under observation phagocytosed Sonazoid microbubbles within 30 minutes. It took 2 to 90 minutes for Kupffer cells to phagocytose microbubbles, and the number of microbubbles phagocytosed by 1 Kupffer cell differed from 1 to 8. The microbubbles inside the Kupffer cells showed high stability and no obvious damage by the Kupffer cell. There were still some intact microbubbles inside the Kupffer cells 24 hours after phagocytosis.

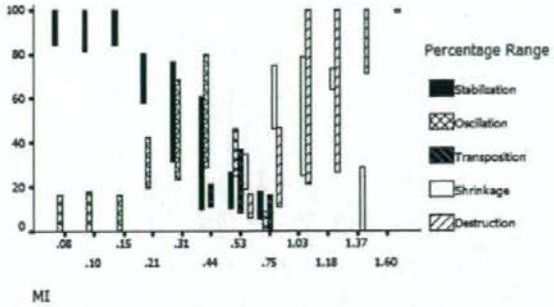

FIGURE 2. Behavior of free microbubbles under high frame rate ultrasound exposure. The percentage range of maintenance of stability drops dramatically from 81.2% to 100% (MI <0.21) to 5.3% to 17.9% (MI = 0.75); for oscillation, the percentage range rises from 0% to 16.1% (MI <0.21) to 28.6% to 80.0% (MI = 0.44); transposition is only seen from MI 0.44 to 0.75; and the percentage ranges of shrinkage and destruction rise from 18.8% to 35% (MI = 0.53) to 46.4% to 75% (MI = 0.75) and from 6.2% to 16.6% (MI = 0.53) to 21.1% to 100% (MI = 1.03), respectively.

Acoustic Behavior of Free Microbubbles

A total of 148 free microbubbles were observed under high frame rate US exposure. The percentage ranges of different kinds of acoustic behavior were shown in Figure 2. When the MI was less than 0.21, 81.2% to 100% of microbubbles remained still under optical observation. With higher energy US exposure (MI from 0.21 to 0.53), the microbubbles categorized as stabilization decreased from 80.4% (MI = 0.21) to 26.8% (MI = 0.53), and those showing oscillation increased from 42.1% (MI = 0.21) to 80.0% (MI = 0.44). At MI = 0.53, the highest percentage (36.8%) of transposition behavior was shown, less than 35% of microbubbles began to shrink, and less than 16.6% of microbubbles began to be destroyed, respectively. At MI = 0.75, the percentage of shrinkage behavior increased to 75%. With MI over 1.03, almost 100% of free microbubbles were destroyed.

A total of 25 free microbubbles were observed under low frame rate US exposure. The percentage ranges of different kinds of acoustic behavior are shown in Figure 3. There were 84.1% to 100% of microbubbles that remained still under optical observation when MI was less than 0.44. The highest percentage (33.3%) of oscillation behavior was shown when MI = 0.53. With even higher energy US exposure (MI from 0.75 to 1.6), the microbubbles appearing stable decreased from 82.3% (MI = 0.75) to 0% (MI = 1.6), and those showing shrinkage increased from 16.6% (MI = 0.75) to 100% (MI = 1.37). The highest percentage (33.3%) of destruction behavior was recorded at MI = 1.6.

Acoustic Behavior of Adherent Microbubbles

A total of 18 and 6 adherent microbubbles were observed under high and low frame rate US exposure, respectively. The percentage ranges of different kinds of acoustic behavior are shown in Figures 4 and 5. No oscillation behavior was shown in adherent microbubbles. For high frame rate

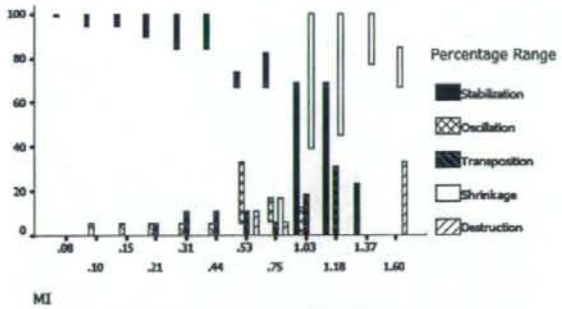

FIGURE 3. Behavior of free microbubbles under low frame rate ultrasound exposure. The percentage range of maintenance of stability is between 84.1% to 100% (MI <0.44), and decreases from 66.7% to 82.3% (MI = 0.75) to 0% (MI = 1.6); the percentage range of oscillation is 0% to 5.3% (MI < 0.53) and highest percentage range (5.3% to 33.3%) is shown at MI = 0.53; percentage range of transposition is 0% to 30.8% between MI 0.21 to 1.18; shrinkage increases from 0% to 16.6% (MI = 0.75) to 76.9% to 100% (MI = 1.37); and the highest percentage (33.3%) of destruction is recorded at MI = 1.6.

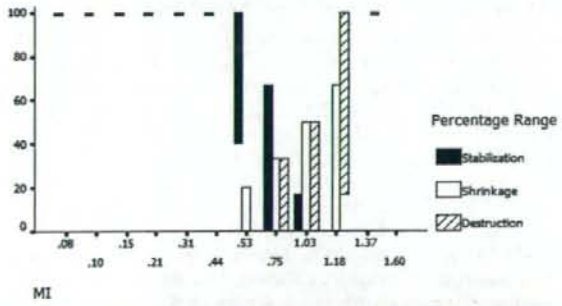

FIGURE 4. Behavior of adherent microbubbles under high frame rate ultrasound exposure. Hundred percent of microbubbles maintain stable when MI <0.53; no oscillation is shown in adherent microbubbles; the percentage range of shrinkage increases from 0% to 33.3% (MI = 0.75) to 0% to 66.7% (MI = 1.18); the percentage range of destruction increases from 0% to 33.3% (MI = 0.75) to 100% (MI = 1.37).

US, all of the microbubbles remained still under optical observation when MI was less than 0.53. Two adherent microbubbles detached from cells and 20% of microbubbles became shrunk at MI = 0.53 (Fig. 6). With even higher US energy (MI from 0.75 to 1.37), the percentage of shrinkage behavior increased from 33.3% (MI = 0.75) to 66.7% (MI = 1.18), and the percentage of destruction behavior increased from 33.3% (MI = 0.75) to 100% (MI = 1.37).

For low frame rate US, all of the microbubbles remained still under optical observation when MI was less than 0.75. With higher US energy, 1 adherent bubble detached from the cell at MI = 1.37, and the percentage of shrinkage behavior increased from 75% (MI = 1.03) to 100% (MI = 1.6), and the percentage of destruction behavior ranged between 25% (MI = 1.6) and 50% (MI = 1.03).

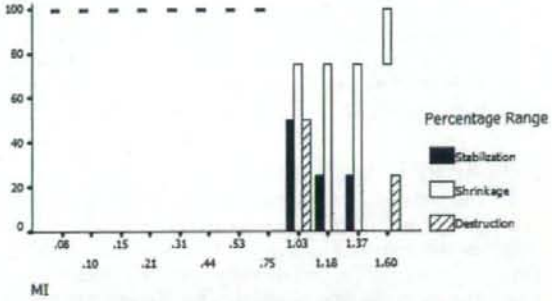

FIGURE 5. Behavior of adherent microbubbles under low frame rate ultrasound exposure. Hundred percent of the microbubbles remain stable when MI <0.75; no oscillation behavior is shown in adherent microbubbles; the percentage range of shrinkage increases from 0% to 75% (MI = 1.03) to 75% to 100% (MI = 1.6); the percentage of destruction ranges between 0% and 25% (MI = 1.6) and 0% and 50% (MI = 1.03).

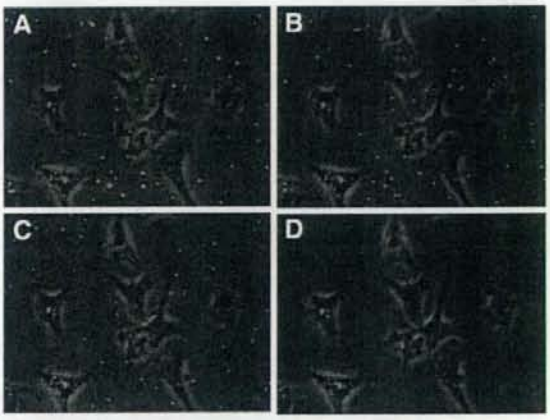

FIGURE 6. Detachment of an adherent microbubble under high frame rate ultrasound insonation. A, The adherent bubble (arrow) shows no significant change under insonation with MI = 0.21; B, bubble (arrow) drops off and moves away slowly (MI = 0.53); C, most of the microbubbles are compressed under insonation with MI = 0.75; and D, all microbubbles are destructed at MI = 1.6.

Acoustic Behavior of Phagocytosed Microbubbles

A total of 21 and 18 phagocytosed microbubbles were observed under high and low frame rate US exposure, respectively. The percentage ranges of different kinds of acoustic behavior are shown in Figures 7 and 8. No oscillation or transposition behavior was seen in phagocytosed microbubbles. For high frame rate US, all of the microbubbles remained still under optical observation when MI was less

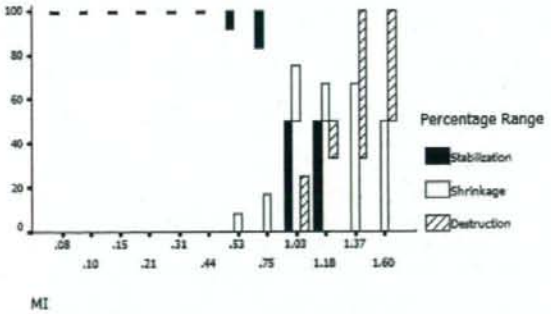

FIGURE 7. Behavior of phagocytosed microbubbles under high frame rate ultrasound exposure. Hundred percent of the microbubbles remain static when MI <0.53; no oscillation or transposition are shown in phagocytosed microbubbles; the percentage range of shrinkage increases from 0% to 8.3% (MI = 0.53) to 50% to 75% (MI = 1.03); and the percentage range of destruction increases from 0% to 25% (MI = 1.03) to 50% to 100% (MI = 1.6).

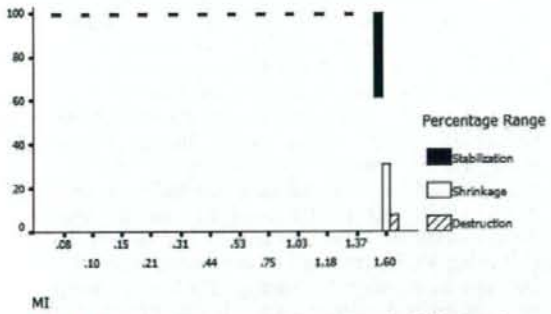

FIGURE 8. Behavior of phagocytosed microbubbles under low frame rate ultrasound exposure. Hundred percent of the microbubbles remain stable when MI <1.6; the percentage ranges of shrinkage and destruction are 0% to 30.8% and 0% to 7.7% at MI = 1.6, respectively.

than 0.53. With higher US energy (MI from 0.53 to 1.6), the percentage of shrinkage behavior increased from 8.3% (MI = 0.53) to 75% (MI = 1.03), and percentage of destruction behavior increased from 25% (MI = 1.03) to 100% (MI = 1.6).

For low frame rate US, all of the microbubbles remained still under optical observation when MI was less than 1.6. The percentage of shrinkage and destruction behavior were 30.8% and 7.7% at MI = 1.6, respectively.

Cell Damage After US Exposure

A total of 32 Kupffer cells were observed under high frame rate US exposure, including 15 Kupffer cells phagocytosed microbubbles, 14 Kupffer cells with microbubbles adhered on, and 3 without any contact with microbubbles. Only 2 Kupffer cells in no contact with microbubbles melted after several seconds of exposure to high-energy US (MI = 1.6). The other cells showed no significant changes of shape during the experiment and 30 minutes after the experiment under microscope observation. There was no significant difference of cell damage after high frame rate US exposure between cells with phagocytosed microbubbles (0 of 15 cells) and without phagocytosed microbubbles (2 of 17 cells) (P = 0.486, Fisher exact test).

With regard to the low frame rate US group, a total of 13 cells were studied, including 10 Kupffer cells phagocytosed microbubbles, 2 Kupffer cells with microbubbles adhered on and 1 without any contacts with microbubbles. No cell damage was found microscopically during or 30 minutes after the experiment. There was no significant difference of cell damage after US exposure between high (2 of 32 cells) and low (0 of 13 cells) frame rate US exposure. (P = 1.000, Fisher exact test).

Measurement of Acoustic Pressure

The acoustic pressure ranges at the level of microbubbles and cells were recorded by hydrophones and oscilloscopes during the US examination. The acoustic pressure was calculated according to the equation of 1 mv = 0.096 MPa after calibrating the hydrophone. The MI displayed on the US scanner linearly correlated with the acoustic pressure at the level of microbubbles and cells measured hydrophonically in this experiment (Fig. 9).

Bubble Behavior Thresholds

According to the behavior of microbubbles under high and low frame rate US exposure, low frame rate US was not as powerful as high frame rate US in effectively inducing of microbubble response. The parameters of high frame rate US in this experiment were similar to the clinical setting of CEUS study. The thresholds for different kinds of microbubble behavior with high frame rate US are shown in Table

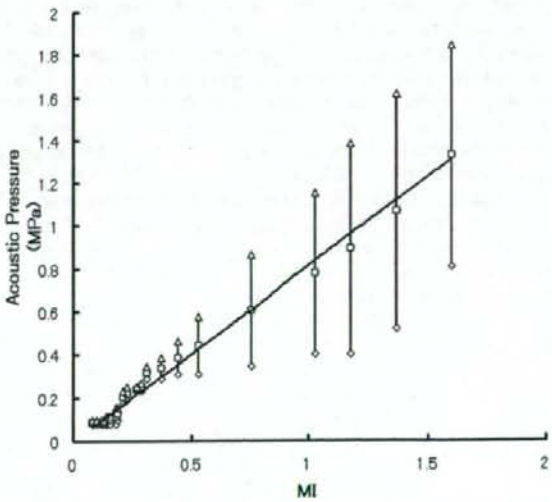

FIGURE 9. MI correlation with the acoustic pressures. MI displayed on the ultrasound scanner shows linear correlation with the acoustic pressure at the level of microbubbles and cells measured by the hydrophone.

TABLE 2. Thresholds for Different Kinds of Microbubble Behavior Under High Frame Rate Ultrasound Exposure

	Free Bubble		Adherent Bubble		Phagocytosed Bubble	
Behavior	MI	Pressure (MPa)	MI	Pressure (MPa)	MI	Pressure (MPa)
Stabilization	0.21	0.1728–0.2304				
Oscillation	0.44	0.3072–0.4608				
Transposition	0.53	0.3072–0.576	0.53	0.3072–0.576		
Shrinkage	0.75	0.3456–0.864	1.03	0.4032–1.152	1.18	0.4032–1.3824
Destruction	1.03	0.4032–1.152	1.18	0.4032–1.3824	1.37	0.5184–1.6128

2. The threshold for free microbubbles to begin oscillation was MI = 0.21; the highest percentage of oscillation behavior was showed at MI = 0.44; MI = 0.53 was most effective for transposition behavior; MI = 0.75 showed the highest percentage of shrinkage behavior; MI = 1.03 was the threshold for complete bubble destruction.

The threshold for adherent microbubbles to detach from the cell surface was MI = 0.53; MI = 1.03 yielded the highest percentage of shrinkage behavior; and MI = 1.18 was the threshold for complete bubble destruction. With regard to the phagocytosed microbubbles, the threshold for microbubbles to be compressed was MI = 1.18; and MI = 1.37 was the threshold for complete bubble destruction.

DISCUSSION

New generation US contrast agents are small air or high-density high-molecular weight gas microbubbles encapsulated by different kinds of shells or stabilized by surface modifying agents.[20] These microbubbles react to external insonation in different ways depending on the properties of the applied US wave, the surrounding liquid properties, and the physical characteristics of the microbubbles, such as the size, shell, resonance frequency, and damping coefficient.[21] Sonazoid is a suspension of perflubutane microbubbles stabilized with thin and flexible phospholipid shells, and have a relatively narrow size distribution, with a median diameter between 2.4 and 3.5 μm. A theoretical model and experimental study predicted the resonance frequencies for optimal perflubutane microbubble sizes would be approximately 2.5, 3.7, and 6.2 μm for 5.0, 3.5, and 2.0 MHz, respectively.[19,22] In the present study, we evaluated the acoustic behavior of perflubutane microbubbles under optical microscopy using a clinical US scanner equipped with a 3.5-MHz microconvex probe and pulse inversion imaging technique.

The relationship between bubble response and the applied acoustic pressure has been described in detail.[21–26] Microbubbles oscillate linearly in relation to low acoustic pressure (<50 kPa) insonation; the pulsations of the microbubbles become nonlinear under moderate acoustic pressure (50–200 kPa); and they rupture and disappear under even higher acoustic pressure (>200 kPa). Bouakaz et al,[26] using encapsulated nitrogen microbubbles and an ultrafast camera, reported that there were 3 different zones depending on the applied US pressure and bubble size. The thresholds for the nondestruction zone and destruction zone were MI <0.3 and MI > 0.6, respectively. In the transient zone, the microbubbles were mainly compressed in the first few cycles, and then the shell fissured and gas escaped after intense shrinkages.

Our results agreed with those findings. Depending on the external acoustic pressure, the free perflubutane microbubbles showed 5 different types of optical behavior which were stabilization, oscillation, transposition, shrinkage, and destruction. With lower acoustic pressure insonation (MI <0.21), over 81% of free microbubbles remained optically stable. The best acoustic pressure range for free microbubbles to oscillate is between MI 0.21 to 0.44. The thresholds for free perflubutane microbubbles to be compressed and destructed was MI = 0.75 and 1.03, respectively. Our thresholds of shrinkage and destruction are relatively higher than previous results, which mainly may be attributable to the smaller size of perflubutane microbubbles (3 μm vs. 4 μm) and higher US frequency (3.5 MHz vs. 1.7 MHz).[26]

Not only the US intensity but also the duration of exposure to US and US frequency influence the response of the microbubbles when they are exposed to US. Walker et al,[27] using 4 different kinds of microbubbles and 3 kinds of US systems, reported that stronger US energy, longer exposure, and lower frequency resulted in significant reductions in both microbubble counts and reflectivity. In the present study, we changed the frame rate of the US from 15 Hz to 1 Hz which decreased the amount of US energy delivered per unit of time. None of the different kinds of microbubbles (free, adherent, and phagocytosed microbubbles) responded effectively to low frame rate US exposure compared with high frame rate at the same MI. All types of microbubble behavior required higher acoustic pressure when low frame rate US was applied, eg, 33% of free microbubbles showed oscillation with low frame rate US at MI = 0.53, compared with 42% of free microbubbles with high frame rate US at MI = 0.21.

The first step for microbubbles to be phagocytosed by Kupffer cells is adhesion to the cell membrane with the help of radiation forces from the external US field and (or) surface receptors such as complement receptors.[10,28] Acoustic behavior of adherent microbubbles is critical for developing and imaging the molecularly targeted US contrast agents which have shown potential ability to provide important information such as inflammatory response, tumor angiogenesis, and thrombus.[9–13] Zhao et al[28] reported that adherent microbubbles with a diameter of 2.3 μm oscillated symmetrically in the plane parallel to the boundary and asymmetrically in the plane perpendicular to the boundary in an external US field with a transmission pressure of 240 KPa. With a higher

transmission pressure of 450 KPa, the center of the microbubble begins to collapse toward the fixed boundary, producing a jet.

From our observation, there were only 3 kinds of acoustic behavior for adherent microbubbles: stabilization, shrinkage, and destruction. Two adherent microbubbles detached from the cells without obvious shrinkage or expansion and became free microbubbles under high frame rate US at MI = 0.53. The detachment of microbubbles from cells may be attributable to the energy of microbubbles oscillation becoming stronger than the adhesive forces from surface receptors and irradiation force of the external US field. Our thresholds for adherent microbubbles to be compressed and destroyed were MI = 1.03 and MI = 1.18, respectively. The adherent microbubbles showed higher thresholds than free microbubbles both for shrinkage and destruction, probably because the cell membranes are flexible enough to slow down the movement of microbubbles and absorb the energy.

Several kinds of microbubbles have been reported to be able to be phagocytosed by Kupffer cells, activated neutrophils, and monocytes.[1,2,10,29,30] The microbubbles phagocytosed by Kupffer cells play an important role in the delayed phase of CUES in the liver by improving the detection and characterization of focal liver lesions.[31,32] The phagocytosed microbubbles also make it possible to noninvasively image areas of inflammation in organ systems and deliver drug or genes into the cells.[10,13–15,29] The acoustic behavior of phagocytosed microbubbles mainly depends on the degree of viscous and thermal dampingm, apart from the properties of external US field.[29,33] Dayton et al[29] reported that the phagocytosed microbubbles experienced a viscous damping approximately 7-fold greater than free microbubbles. Oscillation of the phagocytosed microbubbles was damped by the viscoelastic properties of the surrounding cellular content, resulting in less change in size and shell damage compared with free microbubbles.

Lindner et al[10] reported that albumin microbubbles phagocytosed by activated neutrophils showed minimal change in bubble size compared with baseline at a low acoustic pressure (−400 KPa). At a moderate acoustic pressure (−940 KPa), individual pulses of US resulted in sequential reductions in microbubble size until destruction was complete. At a high acoustic pressure (−1600 KPa), microbubbles were destroyed by a single US pulse. Takeuchi et al[30] also investigated the stability of phospholipid-stabilized and albumin shell microbubbles phagocytosed by activated leukocytes under US insonation. They found the size remained nearly unchanged for both phagocytosed microbubbles and free phospholipid-stabilized microbubbles after insonation at −540 KPa, whereas the volume of free albumin shell microbubbles showed a significant decline. At −1340 KPa, free or phagocytosed albumin shell microbubbles completely deflated at the first or second pulse, whereas there were only limited reductions in volumes of free and phagocytosed phospholipid-stabilized microbubbles.

In the present study, the phagocytosed microbubbles showed much higher thresholds for compression (MI = 1.18) and destruction (MI = 1.37) than both free and adherent microbubbles, which may be attributable to the greater viscous damping from the surrounding cytoplasm. Contrary to the previous leukocyte studies showing that high acoustic pressure frequently caused distortion or immediate rupture of the cell membranes within seconds of microbubble destruction,[10,29,30] no cell lysis was found in the present study after microbubbles were destroyed inside the Kupffer cells. The reason may ascribe to that Kupffer cells are much larger than neutrophils, which enable microbubbles more space to expand under insonation. In addition, it was reported that the percentage of Kupffer cells taking up perflubutane microbubbles was about 1% at clinical doses when the homogeneous hepatic contrast was observed from an animal in vivo study.[2] We therefore think it is not necessary to worry about cell damage after bubble destruction inside Kupffer cells in vivo at acoustic pressures generated by diagnostic US systems in clinical practice.

Although we have described different kinds of optical behavior of free, adherent, and phagocytosed Sonazoid microbubbles, and measured the corresponding thresholds of acoustic pressure under US insonation using similar settings with clinical CEUS examination according to our preliminary observation, these results should be interpreted carefully because of some limitations in our study. First, the distribution of the acoustic energy within the custom-designed experimental setting was very complicated and difficult to control in the present study. The acoustic energy we measured was at the level of microbubbles and cells. Therefore, it may be different from the real acoustic energy emitted from the US probe directly. Second, the relatively small number of microbubbles and Kupffer cells we observed in the present study may limit our results. However, we think the data in our article are enough to show the tendency of different kinds of microbubble behavior under US insonation. Further study is necessary for more precise conclusions. Third, we only evaluated cell damages by optical microscopic findings, but a more precise test, such as LDH leakage is necessary to evaluate the minor damage to the cells. Finally, we have to point out that the properties of acoustic field and the surrounding liquid in the present study cannot be the same as in vivo condition, thus the acoustic behavior of microbubbles in clinical CEUS examination might be different with our in vitro observation.

In conclusion, perflubutane microbubbles (free microbubbles, adherent microbubbles, and the phagocytosed microbubbles) respond to external US insonation according to the acoustic pressure, and behave as stabilization, oscillation, transposition, shrinkage, and destruction. For free microbubbles, the best acoustic pressure range for oscillation is between MI 0.21 to 0.44, which should be recommended for use in clinical real time CEUS procedures. Adherent and phagocytosed microbubbles respond with shrinkage and destruction under higher acoustic pressure (MI from 1.03 to 1.37) without obvious detrimental effect to Kupffer cells, which may be potentially useful for further molecular imaging and drug or gene transportation.

ACKNOWLEDGMENTS

The authors thank Professor J. Patrick Barron of the International Medical Communications Center of Tokyo Medi-

cal University for his review of this manuscript and Associate Professor, Kiyoshi Yoshinaka from Department of Bioengineering, School of Engineering, The University of Tokyo, for helping with hydrophone measurement in the experiment.

REFERENCES

1. Yanagisawa K, Moriyasu F, Miyahara T, et al. Phagocytosis of ultrasound contrast agent microbubbles by Kupffer cells. *Ultrasound Med Biol.* 2007;33:318–325.
2. Watanabe R, Matsumura M, Munemasa T, et al. Mechanism of hepatic parenchyma-specific contrast of microbubble-based contrast agent for ultrasonography: microscopic studies in rat liver. *Invest Radiol.* 2007; 42:643–651.
3. Iijima H, Moriyasu F, Miyahara T, et al. Ultrasound contrast agent, Levovist microbubbles are phagocytosed by Kupffer cells-In vitro and in vivo studies. *Hepatol Res.* 2006;35:235–237.
4. Burns P, Powers J, Hope Simpson UD, et al. Harmonic Imaging: principles and preliminary results. *Angiology.* 1996;47:S63–S74.
5. Averkiou M, Powers J, Skyba D, et al. Ultrasound contrast imaging research. *Ultrasound Q.* 2003;19:27–37.
6. Claudon M, Cosgrove D, Albrecht T, et al. Guidelines and good clinical practice recommendations for contrast enhanced ultrasound (CEUS)–Update 2008. *Ultraschall Med.* 2008;29:28–44.
7. Quaia E, Caliada F, Bertolotto M, et al. Characterization of focal liver lesions with contrast-specific US modes and a sulfur hexafluoride-filled microbubble contrast agent: diagnostic performance and confidence. *Radiology.* 2004;232:420–430.
8. von Herbay A, Vogt C, Willers R, et al. Real-time imaging with the sonographic contrast agent SonoVue: differentiation between benign and malignant hepatic lesions. *J Ultrasound Med.* 2004;23:1557–1568.
9. Palmowski M, Morgenstern B, Hauff P, et al. Pharmacodynamics of streptavidin-coated cyanoacrylate microbubbles designed for molecular ultrasound imaging. *Invest Radiol.* 2008;43:162–169.
10. Lindner JR, Dayton PA, Coggins MP, et al. Noninvasive imaging of inflammation by ultrasound detection of phagocytosed microbubbles. *Circulation.* 2000;102:531–538.
11. Leong-Poi H, Christiansen J, Klibanov AL, et al. Noninvasive assessment of angiogenesis by ultrasound and microbubbles targeted to alpha(v)-integrins. *Circulation.* 2003;107:455–460.
12. Weller GE, Wong MK, Modzelewski RA, et al. Ultrasonic imaging of tumor angiogenesis using contrast microbubbles targeted via the tumor-binding peptide arginine-arginine-leucine. *Cancer Res.* 2005;65:533–539.
13. Christiansen JP, Leong-Poi H, Klibanov AL, et al. Noninvasive imaging of myocardial reperfusion injury using leukocyte-targeted contrast echocardiography. *Circulation.* 2002;105:1764–1767.
14. Christiansen JP, French BA, Klibanov AL, et al. Targeted tissue transfection with ultrasound destruction of plasmid-bearing cationic microbubbles. *Ultrasound Med Biol.* 2003;29:1759–1767.
15. Lu QL, Liang HD, Partridge T, et al. Microbubble ultrasound improves the efficiency of gene transduction in skeletal muscle in vivo with reduced tissue damage. *Gene Ther.* 2003;10:396–405.
16. Song J, Qi M, Kaul S, et al. Stimulation of arteriogenesis in skeletal muscle by microbubble destruction with ultrasound. *Circulation.* 2002; 106:1550–1555.
17. Imada T, Tatsumi T, Mori Y, et al. Targeted delivery of bone marrow mononuclear cells by ultrasound destruction of microbubbles induces both angiogenesis and arteriogenesis response. *Arterioscler Thromb Vasc Biol.* 2005;25:2128–2134.
18. Kubo S, Rodriguez T Jr, Roh MS, et al. Stimulation of phagocytic activity of murine Lupffer cells by tuftsin. *Hepatology.* 1994;19:1044–1049.
19. Sontum PC, Ostensen J, Dyrstad K, et al. Acoustic properties of NC100100 and their relation with the microbubble size distribution. *Invest Radiol.* 1999;34:268–275.
20. Raisinghani A, DeMaria AN. Physical principles of microbubble ultrasound contrast agents. *Am J Cardiol.* 2002;90:3J–7J.
21. de Jong N, Bouakaz A, Frinking P. Basic acoustic properties of microbubbles. *Echocardiography.* 2002;19:229–240.
22. de Jong N, Hoff L, Skotland T, et al. Absorption and scatter of encapsulated gas filled microspheres: theoretical considerations and some measurements. *Ultrasonics.* 1992;30:95–103.
23. Wei K, Skyba DM, Firschke C, et al. Interactions between microbubbles and ultrasound: in vitro and in vivo observations. *J Am Coll Cardiol.* 1997;29:1081–1088.
24. Frinking PJ, de Jong N, Cespedes EI. Scattering properties of encapsulated gas microbubbles at high ultrasound pressures. *J Acoust Soc Am.* 1999;105:1989–1996.
25. Casciaro S, Errico RP, Conversano F, et al. Experimental investigations of nonlinearities and destruction mechanisms of an experimental phospholipid-based ultrasound contrast agent. *Invest Radiol.* 2007;42:95–104.
26. Bouakaz A, Versluis M, de Jong N. High-speed optical observations of contrast agent destruction. *Ultrasound Med Biol.* 2005;31:391–399.
27. Walker KW, Pantely GA, Sahn DJ. Ultrasound-mediated destruction of contrast agents. Effect of ultrasound intensity, exposure, and frequency. *Invest Radiol.* 1997;32:728–734.
28. Zhao S, Ferrara KW, Dayton PA. Asymmetric oscillation of adherent targeted ultrasound contrast agents. *Appl Phys Lett.* 2005;87:nihms8459.
29. Dayton PA, Chomas JE, Lum AF, et al. Optical and acoustical dynamics of microbubble contrast agents inside neutrophils. *Biophys J.* 2001;80: 1547–1556.
30. Takeuchi H, Ohmori K, Kondo I, et al. Interaction with leukocytes: phospholipid-stabilized versus albumin-shell microbubbles. *Radiology.* 2004;230:735–742.
31. Forsberg F, Piccoli CW, Liu JB, et al. Hepatic tumor detection: MR imaging and conventional US versus pulse-inversion harmonic US of NC100100 during its reticuloendothelial system-specific phase. *Radiology.* 2002;222:824–829.
32. Watanabe R, Matsumura M, Chen CJ, et al. Characterization of tumor imaging with microbubble-based ultrasound contrast agent, sonazoid, in rabbit liver. *Biol Pharm Bull.* 2005;28:972–977.
33. de Jong N, Ten Cate FJ, Lancee CT, et al. Principles and recent developments in ultrasound contrast agents. *Ultrasonics.* 1991;29:324–330.

Computer-aided diagnosis for the classification of focal liver lesions by use of contrast-enhanced ultrasonography

Junji Shiraishi[a)]
Kurt Rossmann Laboratories for Radiologic Image Research, Department of Radiology, The University of Chicago, Chicago, Illinois 60637

Katsutoshi Sugimoto and Fuminori Moriyasu
Department of Gastroenterology and Hepatology, Tokyo Medical University, Tokyo, Japan 160-0023

Naohisa Kamiyama
Toshiba Medical Systems Corporation, Otawara, Japan 324-0036

Kunio Doi
Kurt Rossmann Laboratories for Radiologic Image Research, Department of Radiology, The University of Chicago, Chicago, Illinois 60637

(Received 13 August 2007; revised 29 January 2008; accepted for publication 24 February 2008; published 10 April 2008)

The authors developed a computer-aided diagnostic (CAD) scheme for classifying focal liver lesions (FLLs) as liver metastasis, hemangioma, and three histologic differentiation types of hepatocellular carcinoma (HCC), by use of microflow imaging (MFI) of contrast-enhanced ultrasonography. One hundred and three FLLs obtained from 97 cases used in this study consisted of 26 metastases (15 hyper- and 11 hypovascularity types), 16 hemangiomas (five hyper- and 11 hypovascularity types) and 61 HCCs: 24 well differentiated (*w*-HCC), 28 moderately differentiated (*m*-HCC), and nine poorly differentiated (*p*-HCC). Pathologies of all cases were determined based on biopsy or surgical specimens. Locations and contours of FLLs on contrast-enhanced images were determined manually by an experienced physician. MFI was obtained with contrast-enhanced low-mechanical-index (MI) pulse subtraction imaging at a fixed plane which included a distinctive cross section of the FLL. In MFI, the inflow high signals in the plane, which were due to the vascular patterns and the contrast agent, were accumulated following flash scanning with a high-MI ultrasound exposure. In the initial step of our computerized scheme, a series of the MFI images was extracted from the original cine clip (AVI format). We applied a smoothing filter and time-sequential running average techniques in order to reduce signal noise on the single MFI image and cyclic noise on the sequential MFI images, respectively. A kidney, vessels, and a liver parenchyma region were segmented automatically by use of the last image of a series of MFI images. The authors estimated time-intensity curves for an FLL by use of a series of the temporally averaged MFI images in order to determine temporal features such as estimated replenishment times at early and delayed phases, flow rates, and peak times. In addition, they extracted morphologic and gray-level image features which were determined based on the physicians' knowledge of the diagnosis of the FLL, such as the size of lesion, vascular patterns, and the presence of hypoechoic regions. They employed a cascade of six independent artificial neural networks (ANNs) by use of extracted temporal and image features for classifying five types of liver diseases. A total of 16 temporal and image features, which were selected from 43 initially extracted features, were used for six different ANNs for making decisions at each decision in the cascade. The ANNs were trained and tested with a leave-one-lesion-out test method. The classification accuracies for the 103 FLLs were 88.5% for metastasis, 93.8% for hemangioma, and 86.9% for all HCCs. In addition, the classification accuracies for histologic differentiation types of HCCs were 79.2% for *w*-HCC, 50.0% for *m*-HCC, and 77.8% for *p*-HCC. The CAD scheme for classifying FLLs by use of the MFI on contrast-enhanced ultrasonography has the potential to improve the diagnostic accuracy in the histologic diagnosis of HCCs and the other liver diseases. © *2008 American Association of Physicists in Medicine.* [DOI: 10.1118/1.2900109]

Key words: hepatocellular carcinoma (HCC), computer-aided diagnosis, focal liver lesions, artificial neural network (ANN), ultrasonography

I. INTRODUCTION

Noninvasive diagnosis of focal liver lesions (FLLs) has been performed based on contrast-enhanced computed tomography[1] (CT) or magnetic resonance imaging (MRI).[2–4] Although the performance of ultrasonography for the detection of FLLs was considered to be poor compared with those

of CT and MRI,[5] recent progress in ultrasonography with contrast agents and pulse-inversion[6] (phase-inversion) imaging techniques allowed real-time assessment of the liver vascularity pattern, and thus, improvement in the diagnostic accuracy for the classification of FLLs.[6–9] For example, Quaia *et al.*[9] reported that the overall diagnostic accuracy for 452 FLLs by use of conventional baseline ultrasonography (*B*-mode and Doppler U.S.) was improved by use of contrast-enhanced ultrasonography from 49% to 85% for reader 1 and from 51% to 88% for reader 2. Although the use of some microbubble contrast agents for diagnosing liver disease in ultrasonography is under investigation in the United States, they have been used widely for liver diagnosis in most countries in Europe, Asia, and Canada.[10,11]

The diagnosis of liver diseases on ultrasonography with microbubble contrast agents has been studied thoroughly.[6,9–25] For example, benign lesions of hemangioma and focal nodular hyperplasia (FNH) consistently showed sustained enhancement such that the mass appeared equal to or greater in echogenicity than the adjacent liver for the duration of the scanning interval, often as long as 4 min.[22] Liver metastasis, which is the most frequent malignant FLL, can be shown as hypovascularity and rim enhancement in contrast-enhanced ultrasonography when the metastases are from breast, lung, and colon cancers.[14]

Among various kinds of liver diseases, hepatocellular carcinoma (HCC) is the most common primary liver cancer, which usually occurs as a complication of chronic liver disease and most often arises in a cirrhotic liver.[26,27] Because accurate and early diagnosis of HCC is essential for treatment, accurate surveillance of patients with liver cirrhosis is of great clinical importance. In order to diagnose HCCs at their early stages, it is important to determine the degree of histologic differentiation in clinical practice. Vascular invasion is one of the most important determinants of tumor grade and also is reported to be correlated with the degree of histologic differentiation.[28] Therefore, the classification of HCCs into three degrees of histologic differentiation, such as well differentiated, moderately differentiated, and poorly differentiated, is important as well as the benign/malignant classification of FLLs. Although HCCs are generally found to be highly vascular lesions in contrast-enhanced ultrasonography with pulse-inversion imaging,[22] it is difficult to classify HCCs according to their degrees of histologic differentiation without the results of pathologic study. Because of the incidence of postoperative complications, severity of postoperative pain, and increase in the number of hospitalized days, it is recommended to use less invasive real-time percutaneous local ablation therapy for the treatment of well differentiated HCC, rather than a partial hepatectomy. Therefore, for performing real-time percutaneous local ablation therapy during ultrasound examination, it would be useful if the histologic differentiation of the HCC were provided to the physician.

The concept and methodology of computer-aided diagnosis (CAD) to assist radiologists in detecting abnormal lesions and improving the classification accuracy of the differential diagnosis have been developed and studied in various radiologic imaging methods.[29,30] CAD may be defined generally as a diagnosis made by physicians who take into account the results of automated computer analysis of medical images. The computer output may be used as a "second opinion" for improving physicians' decision-making and avoiding oversights. Although there were several studies on CAD schemes for the classification of liver lesions by use of CT and MR images,[31,32] to the best of our knowledge, there has been no application of a CAD scheme for the classification of FLLs in ultrasonography.

In this study, we developed a CAD scheme for classifying FLLs into liver metastasis, hemangioma, and three histologic differentiation types of HCC, by use of microflow imaging (MFI™, Toshiba Medical Systems Corp., Japan) in contrast-enhanced ultrasonography.

II. MATERIAL AND METHODS

II.A. Microflow imaging with contrast-enhanced ultrasonography

In contrast-enhanced ultrasonography, it is possible to obtain a series of enhanced blood flow images continuously in a low-power imaging mode. In the flash-replenishment (FR) method,[33] the microbubbles in the scan volume are destroyed by a burst scan at high-mechanical-index (MI) transmission. The microbubbles in the scan volume are then replenished in the low-MI imaging mode. This concept was first used in myocardial perfusion in high-MI imaging mode by Wei *et al.*,[34] and successful quantitative results were demonstrated.

On the other hand, for observing the structure of the minute vessels, the usefulness of a max-hold imaging technique has been demonstrated by Burns[35] and by Powers *et al.*[36] Microflow imaging (MFI) is an imaging method combining the FR method and a max-hold imaging technique. Figure 1 is a schematic illustration of the MFI procedure and provides sample images in each step. The scanning plane which included the largest and most conspicuous section of the FLL was determined initially by use of conventional *B*-mode scans. Then a contrast agent was injected as a 1.5 ml bolus into an antecubital vein with a 21-gauge peripheral intravenous cannula. During the arterial phase of the contrast enhancement, which was timed for 45 s after the injection, the location of the scanning plane and the size of a field of view were adjusted suitably by use of harmonic imaging (commercially named pulse subtraction). The sequence of MFI was started with the patient's breath-hold and a burst scan with high-MI (1.3–1.6) scanning of five frames. Just after the burst scan, FR low-MI (0.07–0.09) scanning was started simultaneously with a max-hold imaging technique so that the maximum brightness on each pixel was maintained and displayed as persistence vision. In MFI, the inflow high signals obtained with the FR method, which were due to the vascular patterns and the contrast agent replenished from the regions adjacent to the scanning plane, were accumulated until the perfusion of inflow high signals was saturated. In this study, we defined an "early phase" and a "delayed phase" in the MFI as a replenishment time for reaching 50% and 98% of the maximum average pixel value within a FLL,

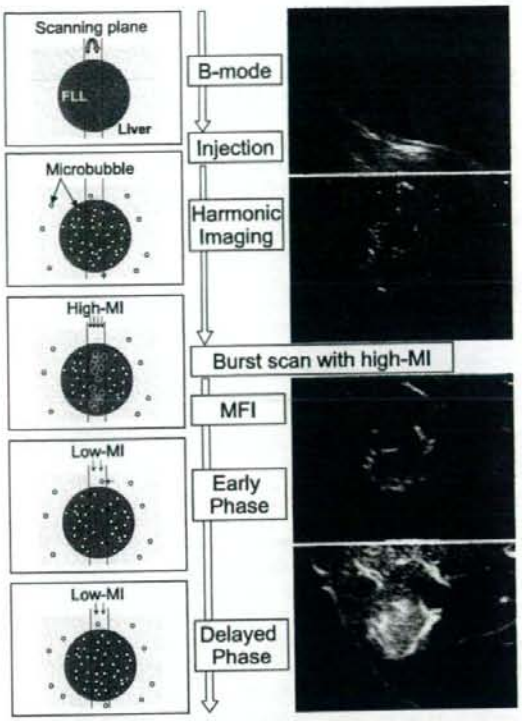

FIG. 1. Illustration of the procedure of MFI and its sample images. Schemas on the left show sections crossing the scanning plane for the MFI. Injected contrast agent (microbubbles) was enhanced by harmonic imaging which depresses the normal structures. Diffused microbubbles in the scanning plane were destroyed by high MI in the first step of MFI, and then the microbubbles in the adjacent region were replenished into the scanning plane corresponding to the vascularity patterns of an FLL. The MFI images were recorded sequentially until the replenishment was saturated.

respectively. In addition, MFI was repeated during the extended portal venous phase (from 45 to 70 s after injection), if necessary.

II.B. Image database

We used 97 MFI cases with 103 FLLs in this study. All cases were collected at the Tokyo Medical University Hospital with IRB-approved patients' consent. The 103 lesions consisted of 26 metastases, 16 hemangiomas, and 61 HCCs: 24 well differentiated (*w*-HCC), 28 moderately differentiated (*m*-HCC), and nine poorly differentiated (*p*-HCC). The 26 metastases and 16 hemangioma lesions were divided into two groups, including hypervascularity (15 metastases, five hemangiomas) and hypovascularity (11 metastases, 11 hemangiomas) types. Pathologies of all cases were determined based on biopsy or surgical specimens. The patient identification information such as patient ID, examination date, gender, and age were blinded to the author so that the patient identification information was secure. Among 97 MFI cases, two cases had multiple lesions of metastases (the numbers of metastases were four and three), and one case had two lesions of HCCs (one *w*-HCC and one *m*-HCC) in the same sequential images of ultrasonography. Locations and approximate contours for the 103 FLLs on contrast-enhanced ultrasonography were determined manually by an experienced physician (K.S.). If one patient had two or more MFI studies for the same lesion in the arterial and portal venous phases, only one MFI study, in which the vascular architecture was most clearly visualized, was selected (by K.S.) and included in the database.

All of the image data for the development of the CAD scheme were originally provided with the AVI format cine clip obtained at the time of examination. All cine clip files had the same format, an 800×600 matrix size and 8-bit gray scale, but with various pixel sizes (mean 0.245 mm, range from 0.109 to 0.416 mm) due to the lesion size and the depth of the lesions from the skin surface. The pixel size for each case was calculated by use of the 1 cm scale displayed in the original cine clip and the number of pixels corresponding to this scale. The acoustic frame rate (AFR) for acquiring ultrasonography was 15 frames per second, and the video frame rate (VFR) for recording image data with the AVI format was 15 or 30 frames per second. The average acquisition time for the MFI was 11.9 s (range from 4.1 to 23.1 s), which depended on the perfusion of the target tissue, and the breath-holding time of the patients during the examination.

In this study, all cases were obtained by use of the ultrasound equipment SSA-770A (Aplio™, Toshiba Medical Systems Corp., Otawara, Japan) with a 3.75 MHz convex transducer (PSK-375BT), with a second generation ultrasound contrast agent, SonoVue™ (Bracco, Milan, Italy). The imaging mode was wide band harmonic imaging with transmission and reception frequencies of 3.75 and 7.5 MHz, respectively.

II.C. Characteristics of FLLs in MFI images

In general, the normal liver is supplied mainly by portal veins, whereas HCCs and hypervascularity metastases are supplied by the hepatic artery as well as tumor vessels. Therefore, from the diagnostic point of view of physicians, enhancement patterns of FLLs in the arterial and portal venous phases of MFI images can be used for characterizing FLLs. For example, the enhancement patterns of the FLL can be described as (1) slow or rapid, (2) uniform or sparse, and (3) strong or weak. In addition, the enhancement patterns of the FLL in the MFI can be distinguished with homogeneous, heterogeneous, centrifugal, and centripetal progressions. The centrifugal and centripetal progressions represent the direction of the enhancement within a FLL such as a change from central to peripheral and another change from peripheral to central, respectively. Figure 2 shows examples of centrifugal and centripetal cases. When two MFI images were compared at the early and the delayed phases, it is apparent that the FLLs were enhanced in two opposite directions, or in no direction. Generally, when only the pulse inversion method was used in the arterial and the portal venous phases of contrast-enhanced ultrasonography, the centripetal progres-

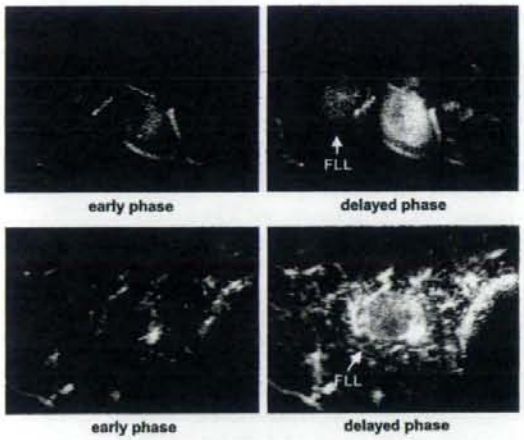

FIG. 2. Examples of two FLLs (*m*-HCCs) which represent centrifugal (upper) and centripetal (lower) progressions of replenishment from early (left) to delayed (right) phases.

sion was typical for hemangioma;[23] however, these patterns were observed occasionally in HCCs on the MFI images.[37]

The comparison of the replenishment pattern of FLLs with those in adjacent liver parenchyma (ALP) regions was also important for characterizing the FLLs on the MFI. By use of this comparison, the FLLs can be classified in three categories, including hyperechoic, hypoechoic, and isoechoic patterns. Figure 3 shows examples of the three patterns of FLLs. We defined hyperechoic when the echogenicity of the FLL was greater than that of the ALP; hypoechoic when the echogenicity of the FLL was less than that of the ALP; and isoechoic when the echogenicity of the FLL was equal to that

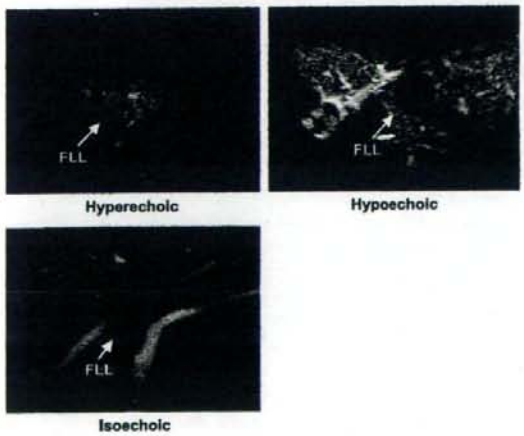

FIG. 3. Examples of three FLLs which represent hyperechoic (upper left: *m*-HCC), hypoechoic (upper right: metastasis), and isoechoic (lower left: *w*-HCC) replenishment patterns.

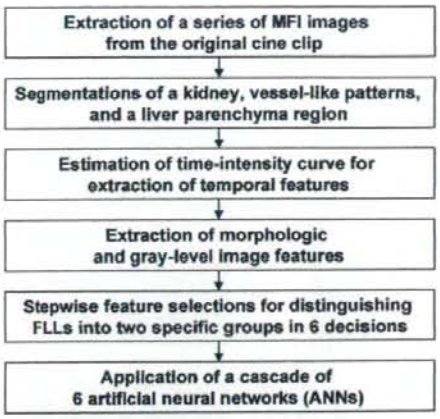

FIG. 4. Overall computerized scheme used in this CAD scheme for the classification of FLLs on MFI images.

of the ALP. The hypoechoic pattern of an FLL in pulse-inversion imaging is shown frequently in cases of hypovascularity metastasis and hemangioma.[9,14,23]

In terms of the diagnostic difficulty for classifying various types FLLs, classifications of hypovascularity lesions including both hemangioma and metastasis were considered to be obvious compared to the classifications of the other hypervascularity lesions because the replenishment pattern of hypovascularity lesions usually indicated a hypoechoic pattern. Among hypervascularity lesions, the classification of hypervascularity hemangioma was relatively obvious because the size of hypervascularity hemangioma was likely to be large compared with the other hypervascularity lesions. The enhancement patterns of *w*-HCC and *p*-HCC were likely to be homogeneous and heterogeneous, respectively, compared to that of *m*-HCC. It has been considered most difficult to distinguish between *m*-HCC and hyper-vascularity metastasis.

II.D. Computerized scheme for classification of FLLs

Figure 4 shows our CAD scheme for the classification of FLLs on contrast-enhanced ultrasonography obtained with MFI. This computerized scheme consists of six major steps, i.e., (1) extraction of a series of MFI images from the original cine clip by application of a smoothing filter and time-sequential running-average techniques; (2) automated segmentations of a kidney, vessel-like patterns, the ALP region, and a central/peripheral region of a FLL; (3) estimation of time-intensity curves for a FLL by use of a series of temporally averaged MFI images for determination of temporal features such as replenishment times at early and delayed phases, flow rate, and peak pixel value; (4) extraction of morphologic and gray-level image features for a FLL; (5) stepwise feature selections for distinguishing two groups in six different decisions; and (6) application of a cascade of independent six artificial neural networks (ANNs) by use of

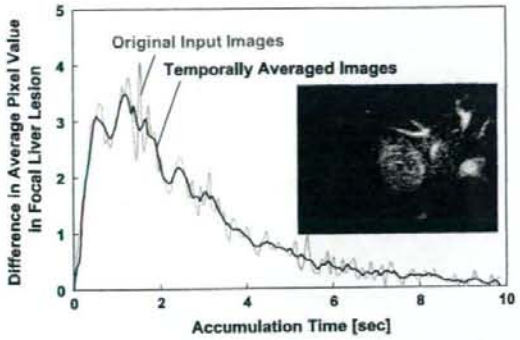

FIG. 5. Difference in average pixel values in sequential MFI images and replenishment times within a FLL (shown in the figure) obtained with the original and temporally averaged MFI images.

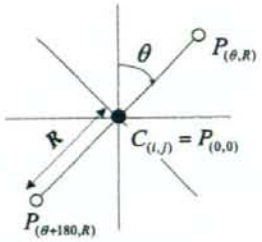

FIG. 6. Explanation of the VE filtering technique for a calculation point $C(i,j)$. $P_{(\theta,R)}$ is a pixel value at the location of $(i+R \sin\theta, j+R \cos\theta)$. The VE filter output $VE(i,j)$ was defined as the maximum value among 12 $P_{(\theta,R)}$ values obtained with four angles of θ and three filter sizes of R.

independently selected features for classifying five types of liver diseases. Details of our computerized scheme are described below.

II.D.1. Extraction of the series of MFI images

In the initial step of our computerized scheme, a series of input images of the MFI was cropped automatically with a 480×360 matrix size, and an 8-bit gray scale with a time interval of 15 frames/s of AFR from the original AVI cine clip which had an 800×600 matrix size with 15 or 30 frames/s of the VFR. The matrix size of 480×360 was determined to exclude completely any patient information displayed on the original cine clip. The time interval in a series of images was standardized with 15 frames/s of AFR by averaging of the series of input images if the original VFR was different from the AFR.

Because ultrasonography has very high time resolution, vascular flows represented in the MFI often had pulsation. In addition, electrical and cyclic signal noises due to harmonic imaging were seen frequently on the images. In order to reduce the signal noise and a cyclic change in pixel values between sequential images, and to enhance temporal changes due to vascularity inside and outside the FLL, we applied a smoothing filter and time-sequential running average techniques, respectively, to the series of input images. We used the smoothing-filter technique with a square kernel size of approximately 1.0 mm in which the matrix size was varied depending on the pixel size. The kernel size of 1.0 mm for the smoothing filter was determined based on the minimum size of the vessels displayed on ultrasound images. In the time-sequential running average technique, we produced a series of temporally averaged images in which a pixel value at each location was averaged with every five sequential frame images (the target frame and each of two frames before and after the target frame). The number of five frames (approximately 0.36 s) for the running average technique was determined because there were approximately three peaks of cyclic change per second in the original sequential frames due to pulsation. Figure 5 shows an example of temporal changes of differences in average pixel values in a FLL obtained with the series of the original input and temporally averaged images. Because the MFI applied a max-hold imaging technique, a rapid increase in the average pixel value at the first 1.0 s could be represented by small cyclic changes by use of temporally averaged images.

II.D.2. Image segmentation

In order to segment a kidney and vessel-like patterns, which often represent very high intensity in contrast-enhanced ultrasonography, from liver parenchyma, we used a multiple-gray-level thresholding[38] and a vessel-like pattern enhancement (VE) filter technique. These segmentations were determined by use of the last image in the series of MFI images with use of the contour of a FLL which was provided by an experienced physician.

A kidney and large vessel-like patterns due to the portal vein and inferior vena cava were initially segmented simply by use of a Gaussian filter and a multiple-gray-level thresholding technique.[38] Multiple-gray-level thresholding of the filtered image was employed for identifying initial candidates for a kidney or large vessel-like patterns. We automatically determined threshold pixel values in each step of the thresholding by use of areas under a histogram within a filtered image, the percentage of which ranged from 0.3% to 33% at high pixel values.[38] In this computerized scheme, initial candidates, which were derived by multiple-gray-level thresholding, were identified as a kidney or large vessel-like patterns if the effective diameter was 6.00 mm or greater.

We used the VE filter technique (Fig. 6), which can enhance and segment vessel-like patterns on the image. The output of the VE filter $VE(i,j)$ at the location of pixel $C(i,j)$ was defined as

$$VE(i,j) = \max_{\theta,R}\{-P_{(\theta,R)} + 2P_{(0,0)} - P_{(\theta+180,R)}\},$$

where $P_{(\theta,R)}$ is a pixel value at the location of $(i+R \sin\theta, j+R \cos\theta)$, and the values of θ (deg) and R (mm) are {0, 45, 90, 135} and {2.0, 4.0, 8.0}, respectively. Thus, the output of the VE filter represented the maximum value among 12 s derivative values that varied with angles and filter sizes. By use of this filter technique, therefore, various sizes of vessel-

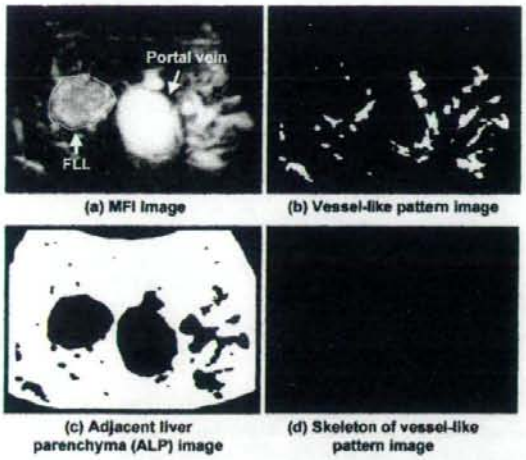

FIG. 7. Example of (a) original MFI image including one FLL (arrow) and a kidney, (b) vessel-like pattern enhanced image obtained with the VE filter technique, (c) segmented ALP regions obtained from the original MFI image, and (d) skeleton of vessel-like pattern enhanced image for estimating the average size of vessel-like patterns on the MFI image.

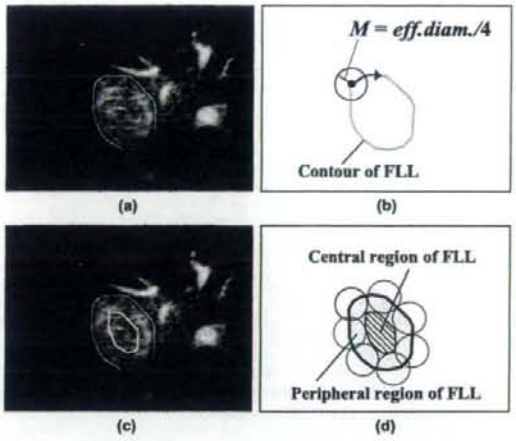

FIG. 8. Sample images of a FLL and illustration of a computerized scheme for dividing the FLL into central and peripheral regions. A fixed margin (M) was calculated from the effective diameter of a FLL and used for dividing the FLL. (a), (c) Original MFI image with a lesion contour which was drawn by the physician, and a contour of the central region segmented by the computer. (b), (d) Peripheral region of a FLL were divided from the central region by use of a rolling circle which has a radius M.

like patterns could be enhanced in either a transverse or a longitudinal section.

An ALP region was determined by use of histogram analysis of the Gaussian-filtered MFI images as well as segmented kidney, vessels, and the contour of an FLL provided by an experienced physician. In this computerized scheme, nonscanned regions in the MFI image were initially excluded by use of the threshold pixel value, which was determined at 2.0% of the maximum pixel value in the MFI image. The regions of segmented kidney, vessel-like patterns, and a FLL were excluded from all of the liver regions for determining ALP regions. Figure 7 shows an example of the original MFI, vessel, ALP, and skeletons of vessel-like pattern images. The purpose and the method of a skeleton of a vessel-like pattern image will be described in Sec. IV.

In addition, we divided a FLL region into central and peripheral regions by use of a fixed margin from the contour of the FLL, as shown in Fig. 8. The size of margin M was determined by a quarter of an effective diameter[39] of the FLL, which was defined with a diameter of a circle that had the same area as the FLL.

II.D.3. Estimation of time-intensity curves

The time-intensity curve with a theoretical model[17,34] for the FLL was estimated by use of average pixel values of the FLL on a series of temporally averaged MFI images. In this model, the time-intensity curve $SI(t)$ was calculated automatically by use of a least-square method for the difference between the average pixel values at the replenishment time t and the theoretical model obtained with the following equation:[17]

$$SI(t) = H_{max}(1 - e^{-\beta t}),$$

where H_{max} represents the peak pixel value in a region of interest, and β is a parameter corresponding to an exponential factor, which can be related to the flow rate in the first phase of the enhancement. By use of this model, temporal features of the peak pixel value H_{max} and the slope factor β of the FLL were determined. In addition to the temporal features, replenishment times at early and delayed phases of the MFI images were determined by use of the estimated time-intensity curve at 50% and 98% of the H_{max} value, respectively. In some specific FLLs such as hemangiomas, pixel values within the FLL were mostly saturated at the early phase and increased very slowly. In order to avoid including such unstable time data, we used 98% of the H_{max} value for the delayed phase instead of the use of 100%. On the other hand, if the estimated replenishment time for the delayed phase was longer than an actual acquisition time due to continuously increasing intensities, the time was determined to be the same as an actual acquisition time.

II.D.4. Extraction of morphologic and gray-level image features

In addition to the temporal features, we extracted morphologic and gray-level image features for the FLL by use of the original and temporally averaged MFI images at the early and delayed phases, and by use of the vessel-like pattern and ALP images.

We obtained three morphologic image features based on the contour of the FLL and a vessel image, such as (1) the